Check for updates

Probing coke formation during the methanol-to-hydrocarbon reaction on zeolite ZSM-5 catalyst at the nanoscale using tip-enhanced fluorescence microscopy†‡

Siiri Bienz, [iD] [a] Sophie H. van Vreeswijk, [iD] [b] Yashashwa Pandey, [iD] [a] Giovanni Luca Bartolomeo, [iD] [a] Bert M. Weckhuysen, [iD] *[b] Renato Zenobi [iD] *[a] and Naresh Kumar [iD] *[a]

The deactivation mechanism of the widely used zeolite ZSM-5 catalysts remains unclear to date due to the lack of analytical techniques with sufficient sensitivity and/or spatial resolution. Herein, a combination of hyperspectral confocal fluorescence microscopy (CFM) and tip-enhanced fluorescence (TEFL) microscopy is used to study the formation of different coke (precursor) species involved in the deactivation of zeolite ZSM-5 during the methanol-to-hydrocarbon (MTH) reaction. CFM submicron-scale imaging shows a preferential formation of graphite-like coke species at the edges of zeolite ZSM-5 crystals within 10 min of the MTH reaction (*i.e.*, working catalyst), whilst the amount of graphite-like coke species uniformly increased over the entire zeolite ZSM-5 surface after 90 min (*i.e.*, deactivated catalyst). Furthermore, TEFL nanoscale imaging with ~35 nm spatial resolution revealed that formation of coke species on the zeolite ZSM-5 surface is non-uniform and a relatively larger amount of coke is formed at the crystal steps, indicating a higher initial catalytic activity.

The global consumption of energy and materials has increased dramatically in recent decades. Currently, a large amount of energy and materials such as plastics and coatings, are produced from fossil resources including natural gas, coal and crude oil.[1] A more sustainable alternative is the production of hydrocarbons by conversion of a methanol feedstock *via* the methanol-to-hydrocarbon (MTH) reaction, which can be fine-tuned to selectively produce olefin (methanol-to-olefin reaction) or gasoline (methanol-to-gasoline reaction) rich products.[2] Since methanol can be obtained from both fossil (*e.g.*, coal and natural gas) as well as non-fossil (*e.g.*, municipal and agricultural waste) carbon sources, the MTH reaction offers a promising solution to make our chemical industry more sustainable.[3] Microporous aluminosilicates, such as zeolite ZSM-5, are widely used solid catalysts in chemical industry to convert methanol to light olefins, aromatics and transportation fuels.[4,5] A zeolite ZSM-5 crystal is composed of straight (0.56×0.53 nm^2) and intersecting sinusoidal (0.55×0.51 nm^2) micropores, which determine the overall product selectivity, whilst Brønsted acid sites provide catalytic activity for the MTH conversion.[6–8] However, besides the desired products, such as light olefins or polyolefins, several undesirable reaction products, such as large coke compounds are also formed.[10–12] The build up of such carbonaceous deposits in the micropores can poison active sites and block pore openings on the surface leading to the deactivation of the solid catalyst.[13,14]

To increase the overall conversion efficiency and prevent subsequent catalyst deactivation, the formation of coke (precursor) compounds needs to be better understood. Coke compounds are a complex mixture of polyaromatic and methylated aromatic species that gradually grow into graphite-like species over time. One possible method to determine the chemical composition of coke compounds is to dissolve them in a suitable solvent and then analyse using techniques such as GC-MS[7] or ^{13}C-NMR.[15] However, this approach cannot identify the insoluble coke species and

[a] Department of Chemistry and Applied Biosciences, ETH Zurich, Vladimir-Prelog-Weg 3, 8093 Zurich, Switzerland. E-mail: zenobi@org.chem.ethz.ch, kumar@org.chem.ethz.ch

[b] Inorganic Chemistry and Catalysis group, Department of Chemistry, Utrecht University, Universiteitsweg 99, 3584 CGUtrecht, The Netherlands. E-mail: b.m.weckhuysen@uu.nl

This journal is © The Royal Society of Chemistry 2022

Catal. Sci. Technol., 2022, **12**, 5795–5801 | 5795

more importantly spatially resolved information on the formation of coke deposits cannot be obtained. Other typical characterization techniques, such as infrared spectroscopy,[16] ultraviolet and visible (UV-vis) spectroscopy,[17,18] Raman spectroscopy[19–21] and fluorescence spectroscopy,[9,22] have a relatively low sensitivity and when employed in a microscopy type operation diffraction-limited spatial resolution, which precludes single-particle analysis at the nanometer length-scale. On the other hand, nanoscale secondary ion mass spectrometry and atomic probe tomography[23] can provide chemical information at the nanoscale, but they are destructive, require time-consuming sample preparation and cannot be used under ambient conditions. Nanoscale chemical characterization has also been demonstrated using photo-induced force microscopy[16] and nanoscale Fourier-transform infrared spectroscopy,[24] however, their use in the field of heterogeneous catalysis is still in its infancy.

In the last two decades, hyperspectral tip-enhanced optical spectroscopy (TEOS) imaging has emerged as a powerful analytical tool for simultaneous topographical and chemical characterization at the nanoscale, in both air and liquid environments.[25,26] In TEOS, a metallic scanning probe microscopy probe is placed in the focal spot of an excitation laser leading to an enormous enhancement and confinement of the electromagnetic field at the probe-apex *via* a combination of localized surface plasmon resonance and lightening rod effect.[27] This highly intense and confined EM field (also called the near-field) enhances optical signals such as Raman,[28–30] photoluminescence,[31–34] or fluorescence[35] from a nanoscopic volume at the contact point of the probe and the sample providing chemical imaging with a nanoscale resolution (Fig. 1).

In this study, we demonstrate that hyperspectral tip-enhanced fluorescence (TEFL) microscopy is a sensitive analytical tool to directly investigate surface coke formation on zeolite ZSM-5 catalysts at the nanoscale. This technique can complement the frequently used characterization tools of zeolite analysis at the bulkscale (*e.g.*, solid-state nuclear magnetic resonance, X-ray diffraction, infrared spectroscopy *etc.*) and at the sub-micron or nanoscale (*e.g.* confocal fluorescence microscopy (CFM), scanning transmission X-ray microscopy, atomic force microscopy (AFM) *etc.*).[36] By investigating zeolite ZSM-5 catalysts, subjected to 10 and 90 min of MTH reaction, we show that hyperspectral CFM allows one to visualize the formation of multiple coke species over the entire zeolite crystal surface at the sub-micron scale, whilst TEFL imaging can be used to zoom into a specific part of the sample and probe coke formation with a spatial resolution of up to 35 nm. Furthermore, TEFL analysis can be performed non-destructively and in a label-free manner under ambient conditions. This work demonstrates the potential of high-resolution TEFL microscopy for studying the deactivation process of industrially relevant heterogeneous catalysts at nanometer length-scales.

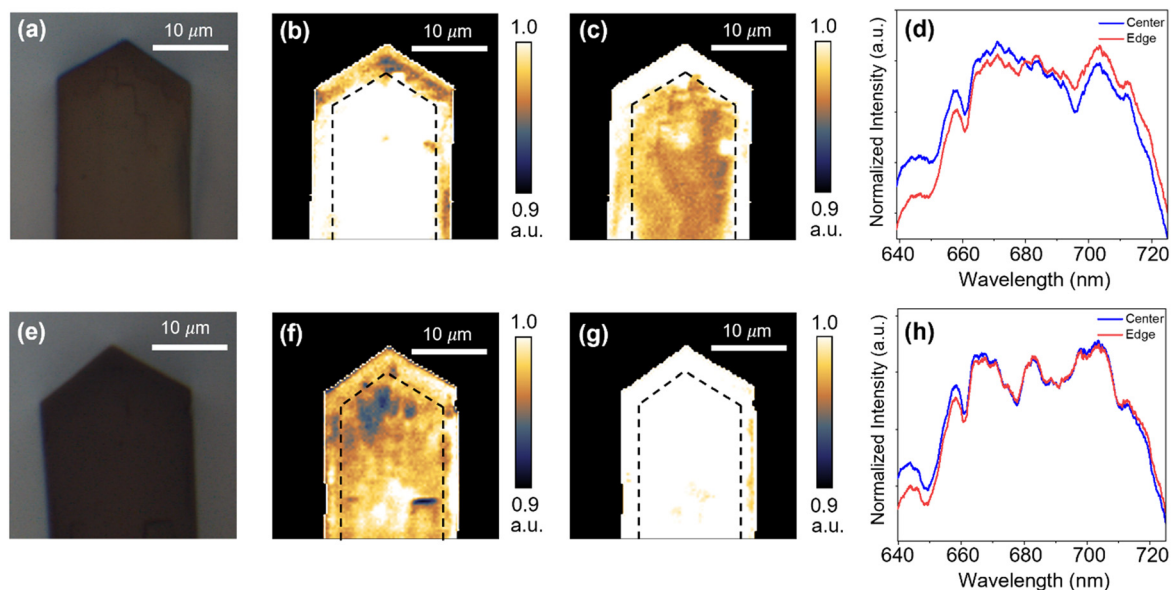# Visualizing coke formation on zeolite ZSM-5 crystals at the microscale

Before performing the MTH reaction, we examined the pristine zeolite ZSM-5 crystals (further labelled as P-ZSM-5) using confocal Raman spectroscopy. An optical image of a transparent zeolite P-ZSM-5 crystal is presented in Fig. S3a,‡ where several step and edge features generated during the crystal growth process can be seen. Raman spectrum of the P-ZSM-5 crystal in Fig. S3b‡ displays the characteristic vibrational modes of the zeolite crystal structure. All Raman bands (Table S1‡) correlate very well with the literature validating the structural integrity of the zeolite P-ZSM-5 crystals used in this study.[37] Notably, no fluorescence signal was detected from the zeolite P-ZSM-5 crystal confirming the absence of any conjugated hydrocarbon species, which could hamper the conclusions from the CFM or TEFL measurements (Fig. 1).

The MTH reaction was performed on the P-ZSM-5 crystals in a Linkam cell at 400 °C using a 10 ml min^{-1} N$_2$ flow through a saturator with methanol. Coke formation on zeolite ZSM-5 crystals subjected to 10 min (further labelled as 10-ZSM-5) and 90 min (further labelled as 90-ZSM-5) of MTH reaction was first investigated using hyperspectral CFM. Based on the optical and UV-vis spectroscopy measurements, shown in Fig. S4 and S5,‡ the 10-ZSM-5 sample represents a working catalyst material containing some coke species, while the 90-ZSM-5 sample represents a deactivated catalyst material, containing a larger amount of graphite-like coke
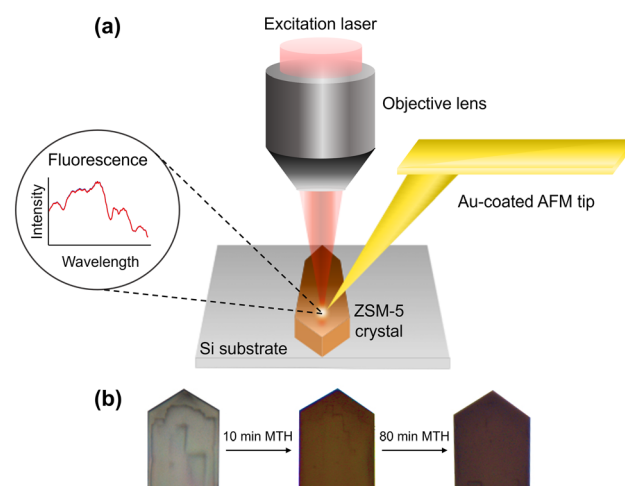
Fig. 1 (a) Schematic diagram of the setup used to study coke formation during the MTH reaction on zeolite ZSM-5 surface at the micro and nanoscale. A detailed scheme of the optical setup is presented in Fig. S1.‡ (b) Optical images of the P-ZSM-5, 10-ZSM-5 and 90-ZSM-5 crystals. With longer time-on-stream (TOS), a darkening of the crystal surface is observed. The large zeolite ZSM-5 crystals used in this study consist of six different 90° rotated neighbouring pyramidal subunits, as shown in Fig. S2.[12,13]‡ In the triangular apex region, due to the rotation of subunits the straight micropores are open to the surface, whereas in the central region, the sinusoidal micropores are open to the surface.[9]

5796 | *Catal. Sci. Technol.*, 2022, **12**, 5795–5801

This journal is © The Royal Society of Chemistry 2022

Fig. 2 (a) Optical image of a 10-ZSM-5 crystal. CFM images of the (b) 640–680 nm and (c) 680–730 nm region intensity. Step size: 300 nm. (d) Plot showing the average of 20 fluorescence spectra measured at the edge (red, region outside the dashed lines in b and c) and center (blue, region inside the dashed lines in b and c) of the 10-ZSM-5 crystal. (e) Optical image of a 90-ZSM-5 crystal. CFM images of the (f) 640–680 nm and (g) 680–730 nm region intensity. Step size: 300 nm. (f) Average of 20 fluorescence spectra measured at the edge (red, region outside the dashed lines in f and g) and center (blue, region inside the dashed lines in f and g) of the 90-ZSM-5 crystal. Spectra in (d) and (h) have been normalized to the signal in the middle of the spectrum at 680 nm.

species on surface. An optical image of a 10-ZSM-5 crystal is shown in Fig. 2a, which appears dark due to the coke species formed during the MTH reaction. It has been shown that conjugated hydrocarbons with longer chains emit fluorescence at longer wavelengths compared to the shorter chain hydrocarbons.[38,39] In order to verify this in our own experimental setup, we measured CFM spectra of the typical coke species formed during the MTH reaction on zeolite ZSM-5 crystals proposed in literature,[40,41] which are plotted in Fig. S6.‡ It can be seen that the small methylated-aromatic coke species, such as hexamethylbenzene, which can typically fit into zeolite micropores[42] indeed have fluorescence emission maximum in the 640–670 nm range. On the other hand, larger, more graphite-like species, such as coronene, which cannot fit into zeolite micropores have fluorescence emission maxima in the relatively higher wavelength range of 680–700 nm.[40,43,44]

To visualize the spatial distribution of smaller and larger coke species on the 10-ZSM-5 crystal surface, CFM images of the 640–680 nm and 680–730 nm band intensity are presented in Fig. 2b and c, respectively. Interestingly, a relatively higher signal intensity is observed at the center of the crystal compared to the edge in Fig. 2b, whilst this trend is reversed in Fig. 2c. This indicates that smaller methylated coke species are more abundantly produced in the center of the crystal, whilst the abundance of larger graphite-like coke species is higher at the edge. This is further confirmed in the comparison of average fluorescence spectra from the edge (red) and central (blue) regions of the 10-ZSM-5 crystal plotted in Fig. 2d. Both spectra show several fluorescence

emission bands confirming the presence of multiple coke species throughout the sample. However, the fluorescence signal in the 680–730 nm range is clearly higher at the edge, indicating a relatively larger amount of graphite-like coke species compared to the center.

The optical image of a 90-ZSM-5 crystal is presented in Fig. 2e, which appears darker compared to the 10-ZSM-5 crystal, presumably due to the presence of a larger amount of coke-type species.[44] CFM images of the 640–680 nm and 680–730 nm band intensity are presented in Fig. 2f and g, respectively. Compared to Fig. 2b and c, no systematic contrast between the edge and central regions is observed in Fig. 2f and g, indicating that both smaller and larger coke species are rather homogeneously distributed over the 90-ZSM-5 crystal surface. This is further confirmed in the averaged spectra from the edge and central regions plotted in Fig. 2h, where no significant difference is observed between the left and right half of the spectra. The significantly less pronounced difference between the edge and center region signifies that with longer TOS, the smaller coke compounds at the center region have time to grow into graphite-like species, causing blocking of the sinusoidal zeolite micropores and subsequent deactivation of the catalyst.

Notably, the average fluorescence spectrum of the 90-ZSM-5 crystal has a different intensity and spectral shape than the 10-ZSM-5 crystal, as shown in Fig. S7a and b,‡ respectively. Surprisingly, a significantly lower fluorescence intensity is observed on the 90-ZSM-5 crystal (Fig. S7a‡). We propose that this is due to the lower penetration of the 632.8 nm

excitation laser caused by the presence of a much thicker coke layer on the 90-ZSM-5 surface and as well as the formation of non-fluorescent coke species. However, the normalized fluorescence spectra, presented in Fig. S7b,‡ reveal a clear shift in the spectral maximum from 670 nm to 700 nm, indicating generation of a relatively higher amount of graphitic coke species with longer TOS.

During the MTH reaction, the preferential accumulation of coke at the triangular apex of the zeolite ZSM-5 crystal compared to the main body has been attributed to the high propensity of pore blocking in the straight channels (Fig. S2‡) due to their smaller size and lower tortuosity.[44–46] However, previous reports did not fully explain the preferential accumulation of coke at the straight edges of the crystal, as observed in Fig. 2c. We propose that the mechanism of coke accumulation at the straight edges is similar to the triangular apex. As schematically shown in Fig. S2,‡ at the straight edges, two pyramidal crystal subunits join to form a boundary. Due to the internal diffusion barrier created at this subunit boundary, movement of smaller methylated aromatic compounds towards the inner region of the crystal is restricted causing them to rapidly grow into graphite-like species. As illustrated in Fig. S2b,‡ the graphite-like species formed at the edge (and subunit boundary) are sampled from a depth of *ca.* 1 μm, which is the probe depth of our confocal optical microscope.

These results demonstrate that hyperspectral confocal imaging can be a powerful tool for spatially resolved detection and simultaneous monitoring of multiple coke species on ZSM-5 zeolite crystals with a sub-micron (~550 nm) spatial resolution.

Visualizing coke formation on zeolite ZSM-5 crystals at the nanoscale

In order to probe the formation of coke compounds at the nanoscale, we performed high-resolution TEFL measurements on the 10-ZSM-5 and 90-ZSM-5 crystals.

Optical image of a 10-ZSM-5 crystal is shown in Fig. 3a. Simultaneously recorded AFM topography and TEFL images measured in an area of 1 μm² in the central region of the crystal (marked in Fig. 3a) are presented in Fig. 3b and c, respectively. Topography image shows a triangular step of height *ca.* 25 nm generated during the inhomogeneous growth of the zeolite ZSM-5 crystal. TEFL image of the full spectrum intensity measured in the same region presented in Fig. 3c also shows a triangular feature, which correlates very well with the topography image. To determine the spatial resolution of the TEFL image, intensity profile along the line across the step in Fig. 3c is plotted in Fig. 3d. The spatial resolution of the TERS image is estimated from the full width at half maximum of a fitted Gaussian curve to be 33.8 nm, which we then safely can set at 35 nm. Interestingly, a relatively higher fluorescence signal is observed at the location of triangular step in the TERS image. Average fluorescence spectra from five regions of high signal intensity (marked with triangles) and five regions of low signal intensity (marked with circles) labelled in Fig. 3c are plotted
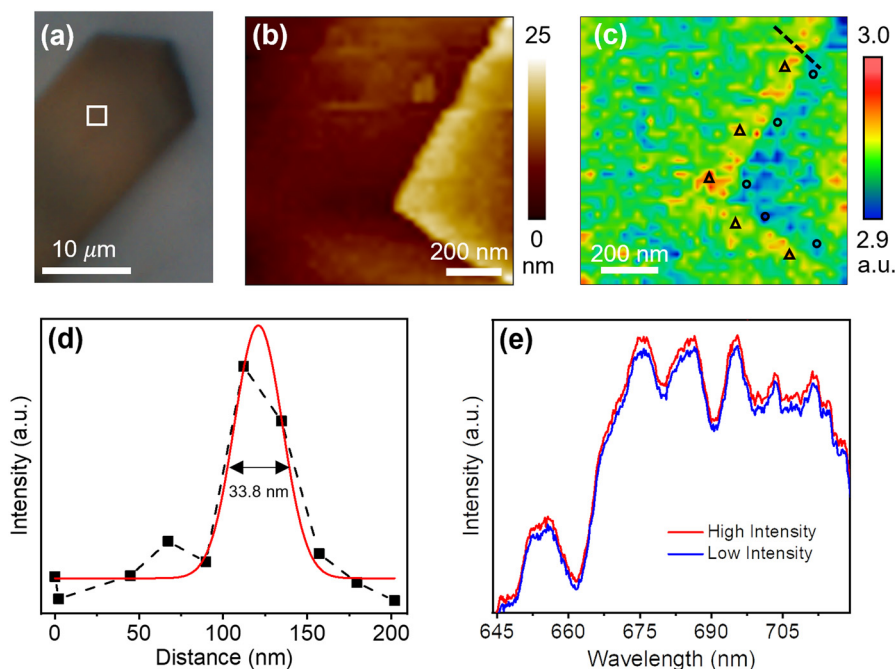
Fig. 3 (a) Optical image of a 10-ZSM-5 crystal. (b) AFM topography image of the 1 μm² area marked in (a). (c) TEFL image of the maximum signal intensity measured simultaneously with the topography image in (b). Step size: 25 nm. (d) Plot of intensity profile along the dotted line marked in (c) with a fitted Gaussian curve (red). (e) Averaged spectra measured at five locations of high and low intensity regions marked with triangles and circles, respectively in (c).

5798 | *Catal. Sci. Technol.,* 2022, **12**, 5795–5801

This journal is © The Royal Society of Chemistry 2022

in Fig. 3e. The shape of the average spectra from high and low signal intensity regions is found to be rather similar indicating that there is no significant difference in the size of coke compounds present at these locations. However, the absolute signal intensity at the step is slightly higher than away from the step signifying a relatively higher catalytic activity. This result suggests that the catalytic activity on the surface of zeolite ZSM-5 crystal is clearly non-uniform at the nanoscale and crystal steps have a relatively higher catalytic activity compared to flat regions. Note that, such subtle differences cannot be observed or spatially resolved by CFM or UV-vis micro-spectroscopy at the nanometer length-scale due to their lower sensitivity and diffraction-limited spatial resolution.

The local differences in coking behavior could arise from the heterogeneous distribution of Al sites. Typically, a Si-rich outer layer (10–200 nm) is followed by a decreasing Al concentration towards the middle (core) of a ZSM-5 crystal.[23,47] We thereby hypothesize that the higher coke formation at the steps on the crystal surface likely results from a relatively higher local density of active Al sites.[23]

We applied the same experimental approach to probe coke formation on the 90-ZSM-5 crystal at the nanoscale. The optical image of a 90-ZSM-5 crystal is shown in Fig. 4a. Simultaneously recorded topography and TEFL intensity images measured in the area marked in Fig. 4a are presented in Fig. 4b and c, respectively. Once again, the TEFL image correlates very well with the topography image confirming

high spatial resolution. The right side of the topography image shows a step of *ca.* 323 nm on the crystal surface. Similar to the TEFL image of 10-ZSM-5 surface, a higher coke formation is observed at the location of the step as shown in Fig. 4c. To visualize this more clearly, average TEFL spectra from five positions of high TEFL intensity and five positions of low TEFL intensity marked in Fig. 4c are presented in Fig. 4d. TEFL signal is found to be clearly higher along the step compared to the flat region, which confirms our earlier observation that at the nanoscale, the ZSM-5 surface exhibits a non-uniform catalytic activity. Particularly, the step features at the crystal surface appear to have a relatively higher amount of coke formation compared to the flat regions. This is the first observation of such nanoscale catalytic heterogeneity at the surface of these zeolite crystals.

A comparison of the normalized averaged spectra from the TEFL images of 10-ZSM-5 and 90-ZSM-5 crystals is presented in Fig. 4e. TEFL spectrum of 90-ZSM-5 clearly shows a higher signal intensity in the 680–730 nm region indicating a higher amount of graphite-like coke species. Notably, these results match quite well with the average CFM spectra of the zeolite 10-ZSM-5 and 90-ZSM-5 crystals presented in Fig. S7b‡ demonstrating that the formation of coke compounds follows the same trend at both micro and nanoscales.

To check if TEFL imaging can differentiate between the type of coke species formed in the center of the ZSM-5 crystal from the edge, we performed TEFL measurement of a 1 μm^2
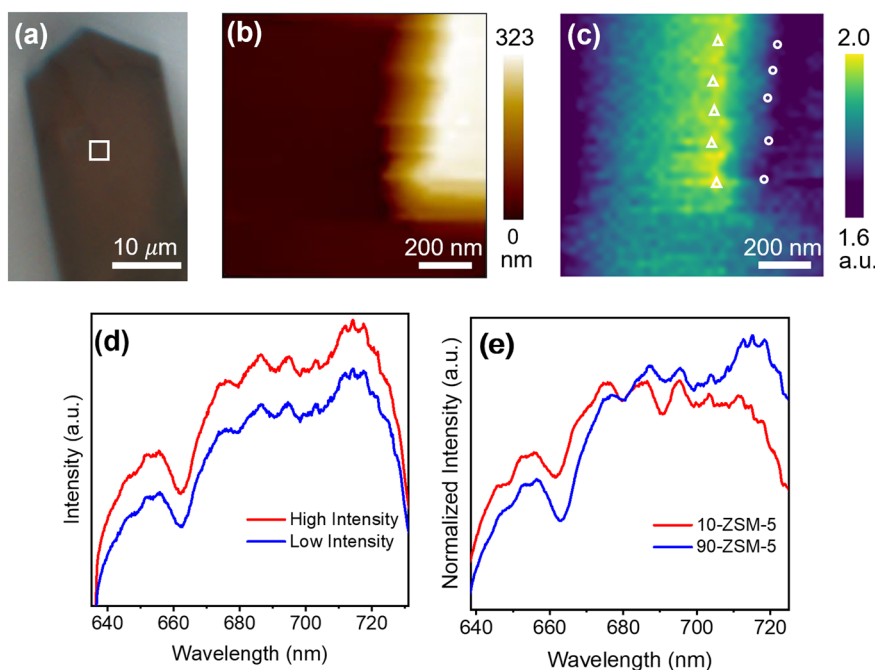
Fig. 4 (a) Optical image of a 90–ZSM-5 crystal. (b) AFM topography image of the 1 μm^2 area marked in (a). (c) TEFL image of the maximum signal intensity measured simultaneously with the topography image in (b). Step size: 25 nm. (d) Averaged TEFL spectra measured at five locations of high and low intensity regions marked with triangles and circles, respectively in (c). (e) Normalized and averaged fluorescence spectra measured in the TEFL images presented in Fig. 3c (red) and 4c (blue). Each spectrum represents an average of 1600 individual TEFL measurements. Both spectra have been normalized to the TEFL signal in the middle of the spectrum at 680 nm.

This journal is © The Royal Society of Chemistry 2022

Catal. Sci. Technol., 2022, **12**, 5795–5801 | **5799**

area at the edge of the 90-ZSM-5 crystal shown in Fig. 4a. A comparison of the average TEFL spectra measured at the central and edge regions is presented in Fig. S8,‡ which show completely different trends. A relatively higher amount of smaller coke species is formed at the edge, whereas the relative abundance of the larger coke species is found to be higher at the center. This indicates that nanoscale TEFL measurements are able to reveal local differences in the type of coke species formed on the ZSM-5 crystal, which may be averaged out in the microscale measurements (Fig. 2f–h). However, a comprehensive investigation of the coke formation at the edge and center would require several more measurements, which we intend to undertake in our future work.

The probe depth of a TEFL signal depends on the optical properties of the sample and is typically limited to a few tens of nm.[31,48] However, the probe depth (estimated from the axial resolution) of CFM in our system is *ca.* 1 μm, which is two orders of magnitude higher than the TEFL probe depth. Therefore, we propose that the TEFL and CFM measurements provide complementary information regarding the formation of coke species on the surface and sub-surface of the ZSM-5 crystals. To illustrate this, Fig. S9a‡ shows a comparison of the average TEFL spectrum measured from the 10-ZSM-5 crystal in Fig. 3 and average CFM spectrum measured in the center of the 10-ZSM-5 crystal in Fig. 2. The two spectral profiles are clearly different, and a close examination indicates a relatively higher amount of larger coke species formation at the surface compared to the subsurface of the ZSM-5 crystals. A similar behavior is observed from the comparison of average TEFL and CFM spectra of the 90-ZSM-5 crystals in Fig. S9b.‡

Conclusions

In summary, we have investigated the formation of coke (precursor) species on the surface of zeolite ZSM-5 catalysts during the MTH reaction at micro- and nano-scales using hyperspectral confocal fluorescence and TEFL chemical imaging. On a zeolite ZSM-5 crystal after 10 min of MTH reaction, which represents a working state of the catalyst, preferential formation of smaller and larger coke species was observed in the center and edge regions of the crystal, respectively. However, after 90 min of MTH reaction, when the catalyst is in its deactivated state, larger graphite-like species were found to cover the entire zeolite crystal surface uniformly. This study also showed the first application of hyperspectral TEFL microscopy to probe coke formation on zeolite ZSM-5 crystals at the nanoscale by recording correlative hyperspectral TEFL and topography images from the working and deactivated catalysts. TEFL imaging with ~35 nm spatial resolution clearly showed that the formation of coke species on both working and deactivated is non-uniform at the nanometer length-scale. Particularly, a relatively larger amount of coke deposits is formed at the steps on the crystal surface, indicating a higher catalytic activity at these locations. This work demonstrates the

potential of combined hyperspectral confocal and tip-enhanced optical microscopy to investigate deactivation processes in the industrially relevant heterogeneous catalysts.

Conflicts of interest

There are no conflicts to declare.

Acknowledgements

Notes and references

1 D. L. Greene, J. L. Hopson and J. Lia, *Transp. Res. Rec.*, 2004, **1880**, 1–9.
2 F. J. Keil, *Microporous Mesoporous Mater.*, 1999, **29**, 49–66.
3 G. A. Olah, *Angew. Chem., Int. Ed.*, 2005, **44**, 2636–2639.
4 W. Wang, Y. Jiang and M. Hunger, *Catal. Today*, 2006, **113**, 102–114.
5 B. Sels and L. Kustov, *Zeolites and Zeolite-like Materials*, Elsevier B.V., Amsterdam, 2016.
6 G. T. Kokotailo, S. L. Lawton, D. H. Olson and W. M. Meier, *Nature*, 1978, **272**, 437–438.
7 H. van Bekkum, E. M. Flanigen, P. A. Jacobs and J. C. Jansen, *Studies in Surface Science and Catalysis*, Elsevier Science, B.V., Amsterdam, 1991.
8 A. Corma, *Chem. Rev.*, 1997, **97**, 2373–2420.
9 M. H. Kox, E. Stavitski, J. C. Groen, J. Perez-Ramirez, F. Kapteijn and B. M. Weckhuysen, *Chem. – Eur. J.*, 2008, **14**, 1718–1725.
10 J. F. Haw and D. M. Marcus, *Top. Catal.*, 2005, **34**, 41–48.
11 J. Li, G. Xiong, Z. Feng, Z. Liu, Q. Xin and C. Li, *Microporous Mesoporous Mater.*, 2000, **39**, 275–280.
12 S. Ilias and A. Bhan, *ACS Catal.*, 2012, **3**, 18–31.
13 D. M. Bibby, N. B. Milestone, J. E. Patterson and L. P. Aldridge, *J. Catal.*, 1986, **97**, 493–502.
14 D. Lesthaeghe, A. Horre, M. Waroquier, G. B. Marin and V. Van Speybroeck, *Chem. – Eur. J.*, 2009, **15**, 10803–10808.
15 C. E. Snape, B. J. McGhee, S. C. Martin and J. M. Amdresen, *Catal. Today*, 1997, **37**, 285–293.
16 D. Fu, K. Park, G. Delen, O. Attila, F. Meirer, D. Nowak, S. Park, J. E. Schmidt and B. M. Weckhuysen, *Chem. Commun.*, 2017, **53**, 13012–13014.
17 J. Goetze, F. Meirer, I. Yarulina, J. Gascon, F. Kapteijn, J. Ruiz-Martinez and B. M. Weckhuysen, *ACS Catal.*, 2017, **7**, 4033–4046.

18 D. Mores, J. Kornatowski, U. Olsbye and B. M. Weckhuysen, *Chem. – Eur. J.*, 2011, **17**, 2874–2884.

19 Y. T. Chua and P. C. Stair, *J. Catal.*, 2003, **213**, 39–46.

20 Y. Yu, G. Xiong, C. Li and F. Xiao, *Microporous Mesoporous Mater.*, 2001, **46**, 23–34.

21 H. An, F. Zhang, Z. Guan, X. Liu, F. Fan and C. Li, *ACS Catal.*, 2018, **8**, 9207–9215.

22 J. P. Hofmann, D. Mores, L. R. Aramburo, S. Teketel, M. Rohnke, J. Janek, U. Olsbye and B. M. Weckhuysen, *Chem. – Eur. J.*, 2013, **19**, 8533–8542.

23 J. E. Schmidt, J. D. Poplawsky, B. Mazumder, O. Attila, D. Fu, D. A. de Winter, F. Meirer, S. R. Bare and B. M. Weckhuysen, *Angew. Chem., Int. Ed.*, 2016, **55**, 11173–11177.

24 F. Huth, A. Govyadinov, S. Amarie, W. Nuansing, F. Keilmann and R. Hillenbrand, *Nano Lett.*, 2012, **12**, 3973–3978.

25 N. Kumar, S. Mignuzzi, W. Su and D. Roy, *EPJ tech. instrum.*, 2015, **2**, 1–23.

26 N. Kumar, W. Su, M. Vesely, B. M. Weckhuysen, A. J. Pollard and A. J. Wain, *Nanoscale*, 2018, **10**, 1815–1824.

27 N. Kumar, B. M. Weckhuysen, A. J. Wain and A. J. Pollard, *Nat. Protoc.*, 2019, **14**, 1169–1193.

28 N. Kumar, B. Stephanidis, R. Zenobi, A. J. Wain and D. Roy, *Nanoscale*, 2015, **7**, 7133–7137.

29 N. Kumar, C. S. Wondergem, A. J. Wain and B. M. Weckhuysen, *J. Phys. Chem. Lett.*, 2019, **10**, 1669–1675.

30 Z. F. Cai, J. P. Merino, W. Fang, N. Kumar, J. O. Richardson, S. De Feyter and R. Zenobi, *J. Am. Chem. Soc.*, 2022, **144**, 538–546.

31 N. Kumar, A. Zoladek-Lemanczyk, A. A. Guilbert, W. Su, S. M. Tuladhar, T. Kirchartz, B. C. Schroeder, I. McCulloch, J. Nelson, D. Roy and F. A. Castro, *Nanoscale*, 2017, **9**, 2723–2731.

32 W. Su, N. Kumar, H. Shu, O. Lancry and M. Chaigneau, *J. Phys. Chem. C*, 2021, **125**, 26883–26891.

33 W. Su, N. Kumar, S. Mignuzzi, J. Crain and D. Roy, *Nanoscale*, 2016, **8**, 10564–10569.

34 J. Shao, F. Chen, W. Su, N. Kumar, Y. Zeng, L. Wu and H. W. Lu, *J. Phys. Chem. Lett.*, 2022, **13**, 3304–3309.

35 N. Kumar, S. Kalirai, A. J. Wain and B. M. Weckhuysen, *ChemCatChem*, 2019, **11**, 417–423.

36 S. H. van Vreeswijk and B. M. Weckhuysen, *Natl. Sci. Rev.*, 2022, **0**, 1–20.

37 O. Attila, H. E. King, F. Meirer and B. M. Weckhuysen, *Chem. – Eur. J.*, 2019, **25**, 7158–7167.

38 G. T. Whiting, F. Meirer, D. Valencia, M. M. Mertens, A. J. Bons, B. M. Weiss, P. A. Stevens, E. de Smit and B. M. Weckhuysen, *Phys. Chem. Chem. Phys.*, 2014, **16**, 21531–21542.

39 M. H. F. Kox, A. Mijovilovich, J. J. H. B. Sättler, E. Stavitski and B. M. Weckhuysen, *ChemCatChem*, 2010, **2**, 564–571.

40 L. Palumbo, F. Bonino, P. Beato, M. Bjorgen, A. Zecchina and S. Bordiga, *J. Phys. Chem. C*, 2008, **26**, 9710–9716.

41 R. Y. Brogaard, B. M. Weckhuysen and J. K. Nørskov, *J. Catal.*, 2013, **300**, 235–241.

42 M. Bjorgen, S. Svelle, F. Joensen, J. Nerlov, S. Kolboe, F. Bonino, L. Palumbo, S. Bordiga and U. Olsbye, *J. Catal.*, 2007, **249**, 195–207.

43 E. C. Nordvang, E. Borodina, J. Ruiz-Martinez, R. Fehrmann and B. M. Weckhuysen, *Chem. – Eur. J.*, 2015, **21**, 17324–17335.

44 D. Mores, E. Stavitski, M. H. Kox, J. Kornatowski, U. Olsbye and B. M. Weckhuysen, *Chem. – Eur. J.*, 2008, **14**, 11320–11327.

45 M. H. F. Kox, E. Stavitski and B. M. Weckhuysen, *Angew. Chem.*, 2007, **119**, 3726–3729.

46 E. Stavitski, M. H. Kox and B. M. Weckhuysen, *Chem. – Eur. J.*, 2007, **13**, 7057–7065.

47 Z. Ristanovic, J. P. Hofmann, U. Deka, T. U. Schulli, M. Rohnke, A. M. Beale and B. M. Weckhuysen, *Angew. Chem., Int. Ed.*, 2013, **52**, 13382–13386.

48 D. Mrdenovic, D. Abbott, V. Mougel, W. Su, N. Kumar and R. Zenobi, *ACS Appl. Mater. Interfaces*, 2022, **14**, 24938–24945.

This journal is © The Royal Society of Chemistry 2022

Catal. Sci. Technol., 2022, **12**, 5795–5801 | **5801**